Journal of Power Sources 541 (2022) 231625

Contents lists available at ScienceDirect

Journal of Power Sources

journal homepage: www.elsevier.com/locate/jpowsour

Metal-supported solid oxide fuel cell system with infiltrated reforming catalyst layer for direct ethanol feed operation

Martinus Dewa[a,b], Mohamed A. Elharati[b], A. Mohammed Hussain[c,**], Yohei Miura[d], Dong Song[d], Yosuke Fukuyama[d], Yoshihisa Furuya[c], Nilesh Dale[c], Xianghui Zhang[b], Oscar G. Marin-Flores[b], Di Wu[b], M. Grant Norton[a,b], Su Ha[b,*]

[a] *School of Mechanical and Materials Engineering, Washington State University, Pullman, WA, 99164, USA*
[b] *The Gene and Linda Voiland School of Chemical Engineering and Bioengineering, Washington State University, Wegner Hall Room 105, 1505, NE Stadium Way, Pullman, WA, 99164, USA*
[c] *Nissan Technical Centre North America, Farmington Hills, MI, 48335, USA*
[d] *Nissan Research Centre, Nissan Motor Corporation Limited, Kanagawa, 237-8523, Japan*

HIGHLIGHTS

- Catalyst infiltration into metal-supported solid oxide fuel cell (MS-SOFC).
- MS-SOFC with the catalyst successfully operates under direct-ethanol feed condition.
- MS-SOFC with the catalyst shows enhanced synthesis gas production rate.
- MS-SOFC with the catalyst offers increased mass transfer limited current density.
- MS-SOFC with the catalyst offers enhanced stability with increased coking resistance.

GRAPHICAL ABSTRACT

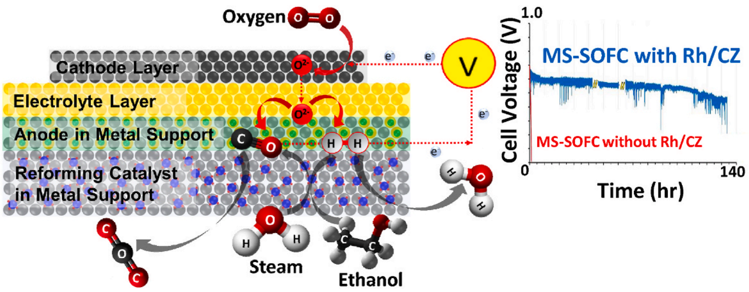

ARTICLE INFO

Keywords:
Metal-supported solid oxide fuel cell
Internal ethanol steam reforming
Ceria-zirconia supported rhodium catalyst
Hydrogen production

ABSTRACT

In this work, we introduce a Rhodium-Ceria-Zirconia (Rh/CZ) internal reforming catalyst layer to a high-performance metal-supported solid oxide fuel cell (MS-SOFC). The catalyst is applied by infiltrating Rh, CeO_2, and ZrO_2 precursors into the stainless steel (SS 430) support. The cell is tested by directly feeding an ethanol solution (45 vol%) into the anode at 600 °C. Our experimental results show that the button cell with the infiltrated 5 wt% Rh/CZ demonstrates an improved performance over the button cell without the catalyst layer by enhancing the internal reforming activity of ethanol toward the production of synthesis gas. The maximum current density improved from 0.3 A cm^{-2} to 0.4 A cm^{-2} while the long-term stability was also greatly improved. Post mortem cell analysis reveals that the infiltrated catalyst layer can prevent severe coke deposition from the cell's anode functional layer. The proposed integrated reforming catalyst and MS-SOFC system is a promising pathway to enable bioethanol fed-SOFC technology for future electric vehicles.

---

[*] Corresponding author.
[**] Corresponding author.
E-mail addresses: hussain.jabbar@nissan-usa.com (A.M. Hussain), suha@wsu.edu (S. Ha).

https://doi.org/10.1016/j.jpowsour.2022.231625
Received 6 February 2022; Received in revised form 28 April 2022; Accepted 12 May 2022
Available online 10 June 2022

1. Introduction

The metal-supported solid oxide fuel cell (MS-SOFC) can endure thermal shock from both rapid start-up and cool-down. Such advantage makes the MS-SOFC more favorable for automobile applications compared to the conventional cermet-based SOFC [1]. A conventional Ni-yttria-stabilized-zirconia (Ni-YSZ) cermet anode-supported cell can undergo reduction-oxidation cycles during its operation. As a result, the cermet anode can experience rapid volumetric changes making it susceptible to cracking [2]. In addition, the metal support used for MS-SOFC is generally made of stainless steel. Therefore, the MS-SOFC arrangement is also more economically viable for commercialization because of its lower materials cost than the Ni-based cermet in a conventional anode-supported cell [3]. The MS-SOFC also excels in terms of fabrication. It generally only requires a single-step sintering process (in the range 1300–1400 °C) followed by a series of wet chemistry infiltration of the anode material precursor at low calcination temperature (typically between 500 and 600 °C). Such an infiltration process allows the anode to form as nanosized particles. The smaller anode particle size increases the triple-phase boundary (TPB) area in the cell and, therefore, can enhance electrochemical performance [3–7].

In general, SOFC technology fueled by hydrogen is a clean and efficient approach to produce electricity. However, the commercialization of hydrogen SOFCs is hindered by the lack of a robust H_2 infrastructure and safety concerns related to storage [8–14]. Since SOFCs can operate at high temperatures (between 600 and 1000 °C) [15], it is possible to utilize logistic liquid fuels such as bioethanol to run the SOFC system. The utilization of logistic liquid fuels can solve hydrogen production, transportation, and storage issues necessary for H_2 SOFCs because of the presence of a well-established infrastructure and safety procedures. A Ni-based anode, such as Ni-YSZ, is an excellent electrode material for SOFCs due to its catalytic activity towards hydrogen oxidation and its high mixed electronic-ionic conductivity. However, the Ni-YSZ anode is susceptible to carbon formation or coking that can permanently deactivate the cell. In a more complex system, such as fuel cell stacks, the carbon deposit can block the fuel channel leading to catastrophic failure [16,17]. Therefore, the anode material for a SOFC system that runs with logistic liquid fuels must also possess high catalytic activity and coking resistance.

In our previous work, we used ethanol to run a conventional cermet-based SOFC. Ethanol can be produced from renewable sources such as lignocellulosic biomass or sugarcane via fermentation processes [18]. Thus, a SOFC system directly operating with biomass-derived ethanol can help address our future energy needs in a sustainable way. In the past, researchers have been trying to directly feed ethanol into a SOFC by substituting the Ni-YSZ for more coking resistant materials, such as Fe–Ni-scandia-stabilized-zirconia (Fe–Ni/ScSZ) [19], Cu–CeO_2-ScSZ [20], or $La_{0.75}Sr_{0.25}Cr_{0.5}Mn_{0.5}O_{3-\delta}$ (LSCM) [21]. However, these alternative anode materials will be difficult to commercialize because they will have to compete with a well-developed and technologically mature Ni-YSZ anode. Furthermore, the limited surface area offered by the anode functional layer would limit its internal reforming activity.

Alternatively, introducing an internal micro-reforming catalyst unit with a high surface area on the anode side of the cell has been recognized as an efficient solution to overcome the coking and low reforming activity of the conventional anode design. Reforming catalyst development to enhance the steam and dry reforming performance in alcohol and other fuels has been extensively studied and reported [22–28]. For an anode with the internal micro-reforming design, ethanol is first reformed into a mixture of H_2 and CO (i.e., synthesis gas) over the high surface area micro-reforming functional layer, followed by electrochemical oxidation over the anode functional layer [29–33]. However, the overall volume and the capital costs of the system will be increased if a physical catalyst layer is applied over the anode or a separate reforming catalyst layer is used. In the MS-SOFC system, the precursor infiltration method is generally used to introduce the anode material. Therefore, the same method can be applied to introduce the reforming catalyst layer while reducing the number of fabrication steps and keeping the system compact [4,34]. Essentially, we can utilize the significant void volume present in the MS-SOFC's porous metal support by infiltrating it with a reforming catalyst precursor. Instead of acting solely as mechanical support, the metal support can now be functionalized as a micro-reforming catalyst layer.

In this work, we investigated the behavior of the reforming catalyst within the metal support. Any interaction between the metal and the anode particles was analyzed because results from cermet-based SOFCs may not be directly applicable to MS-SOFCs since they are structurally different. During the cell test, electrochemical and reforming performances were measured. Post-test analyses were also conducted to determine cell integrity and the degree of coking on the spent MS-SOFCs.

In our past work, we have demonstrated that applying a 5 wt% Rh/CZ catalyst as a micro-reforming layer on the conventional Ni-YSZ anode can effectively improve the cell's maximum current density, durability, and coking resistance under the feeding condition of 35 vol% ethanol solution fuel (S/C ratio = 3) and a flow rate of 5 ml h^{-1} [18]. Even though 5 wt% Rh/CZ is expensive due to its high noble metal content, there are not many reforming catalysts that can perform well under such severe coking conditions. Generally, a lower steam to carbon ratio is preferable to obtain a higher fuel efficiency. However, steam is required as a reforming agent and to suppress coking formation. Therefore, finding the right balance between the steam and ethanol (steam to carbon ratio) is essential [35]. In this work, we used the infiltrated 5 wt% Rh/CZ as a reference reforming catalyst in our MS-SOFC test under the feeding condition of 45 vol% ethanol solution fuel (S/C ratio = 2) at 600 °C. Hence, the operating condition used in this study with an MS-SOFC is harsher than that used in our previous studies with ceramic-based SOFCs.

Water is formed on the anode surface as the reaction product during fuel cell operation. Since our infiltrated catalyst is located within the metal support or in very close proximity to the anode functional layer, our infiltrated catalyst can immediately utilize this additional water from the fuel cell reaction to prevent coke formation. On the other hand, if the catalyst is located far away from the cell's functional layer (as in a separate reformer unit or painted on the anode surface), the catalyst will not be able to effectively harness this additional water provided by the fuel cell reaction. Therefore, the infiltrated catalyst configuration in the current work can allow us to operate the cell in harsher conditions (i.e., a lower S/C ratio).

The objective of the present study is to investigate an MS-SOFC system that operates at an intermediate temperature (600–700 °C). A lower operating temperature is preferred because it requires less energy for a start-up. Unlike a conventional ceramic-supported SOFC, our MS-SOFC has stainless steel support. Stainless steel tends to oxidize if exposed to high temperatures. Therefore, testing at a temperature >700 °C is avoided. On the other hand, an operating temperature lower than 600 °C leads to a low cell performance due to the high ohmic resistance of the electrolyte and poor oxygen reduction activity at the cathode. Thus, this present study focuses on the cell performance at 600 °C where thermal stability and activity are balanced. Additionally, 600 °C is thermodynamically more favorable to form coking than 650 and 700 °C. By operating our MS-SOFC at 600 °C, we can more effectively investigate its coking resistance.

2. Experimental

2.1. Half cell fabrication

The MS-SOFC fabrication steps are shown in Fig. 1. The stainless steel 430 support was tape cast to form a porous metal layer with a thickness of 300 μm and diameter of 25 mm. A porous scandia-yttria stabilized zirconia (Sc/YSZ) was tape cast on top of the metal support as a scaffold layer for the subsequent anode infiltration process. A dense Sc/YSZ electrolyte layer was coated on the scaffold layer. This green cell was co-sintered under a reducing atmosphere at 1350 °C. The sintered half-cell was then infiltrated with the anode catalyst nickel-gadolinium doped ceria (Ni/GDC) to occupy pores within the Sc/YSZ scaffold. The cell was then heat-treated at 600 °C to calcine the infiltrated Ni/GDC anode.

2.2. Reforming catalyst synthesis and characterization

The catalytic activity for ethanol steam reforming (ESR) was initially performed on a YSZ pellet infiltrated with the 5 wt% Rh/CZ precursors. The pellet was fabricated via dry pressing. A 75 wt% 8-YSZ powder (Tosoh Corp.) was ball milled with 25 wt% PMMA powder (Sunjin). The composite powder was then dry pressed to form a pellet with a diameter of 11.6 mm and a thickness of 1.15 mm. The pressed pellet was sintered at 1400 °C for 4 h using a heating rate of 3 °C min^{-1}. For the infiltration process, $RhCl_3{\cdot}xH_2O$ (Alfa Aesar), $Ce(NO_3)_3{\cdot}6H_2O$ (Alfa Aesar), and $ZrO(NO_3){\cdot}xH_2O$ (Alfa Aesar) precursors were mixed in a stoichiometric ratio (0.7 Ce: 0.3 Zr) with 5 wt % of Rh and dissolved in 10 ml of methanol using an ultrasonicator. A 50 μl aliquot of this precursor solution was infiltrated on the YSZ scaffold 25 times. The catalyst was calcined at 600 °C over 4 h after every 5 infiltrations. The calcined catalyst was then reduced at 800 °C under 80 sccm of H_2 and 20 sccm of Ar for 6 h. The resulting catalyst is referred to as Rh/CZ. Pure Rh precursor without the CZ precursors was also infiltrated into the YSZ pellet for comparison purposes. The ESR test setup is shown in Fig. S.1. The YSZ pellet (with and without catalyst precursors) was embedded on the stainless steel mesh (Cleveland Wire Cloth & Manufacturing Co). The pellet was sealed with ceramic sealant Ceramabond 552 (AREMCO) on top of the alumina tube. The setup was heated by an electric tube furnace to 800 °C using a heating rate of 1.5 °C min^{-1}. During the heating process, 50 sccm of N_2 flowed into the pellet. After reaching 800 °C, a flow of 50 sccm of H_2 for 1 h was used to reduce the Rh particles in the pellet. After the reduction process, 45 vol% aqueous ethanol solution equal to a steam-to-carbon molar (S/C) ratio of 2 was introduced using a calibrated peristaltic pump with 50 sccm of N_2 as the carrier gas. A chiller trapped the condensates such as water and unreacted ethanol at 4 °C. The dry gases were analyzed by a gas chromatograph equipped with a TCD detector and two packed columns (Molecular Sieve 13X and HayeSep D). The catalytic activity was measured at 600–800 °C. Carbon conversion and syngas production were calculated as follow:

$$Carbon\ Conversion = \frac{moles\ of\ produced\ (CO + CO_2 + CH_4)}{2 \times\ moles\ of\ ethanol\ fed} \times 100\% \tag{1}$$

$$H_2\ production = H_2\ concentration \times total\ dry\ gas\ flow\ rate\ \times 100\% \tag{2}$$

$$CO\ production = CO\ concentration \times total\ dry\ gas\ flow\ rate\ \times 100\% \tag{3}$$

Following the catalytic activity test of infiltrated 5 wt% Rh/CZ on a YSZ scaffold toward the ESR, the 5 wt% Rh/CZ precursors were infiltrated into a porous stainless steel support 25 times using the previously mentioned method.

Crystalline phases of the 5 wt% Rh/CZ catalyst were determined using a Rigaku (Miniflex 600) with Cu Kα radiation. X-ray diffraction (XRD) analysis was performed at 40 kV and 15 mA in steps of 0.01° with a scanning rate at 1 °C min^{-1} from 10° to 75°. Peak analysis was performed using PDXL2 database software. In addition, scanning electron microscopy (SEM) and energy dispersive spectroscopy (EDS) of the infiltrated metal support were conducted using an Apreo VolumeScope™.

2.3. Cell testing

The MS-SOFC test procedure was started by infiltrating the 5 wt% Rh/CZ precursors into the metal support at the anode surface using the previously mentioned method. Platinum mesh and wire (Aldrich) were used as the current collector. The catalyst and electron collector applications are shown in Fig. S.2. The anode surface was polished using sandpaper and then spot welded with the Pt mesh. The cathode layer was deposited over the electrolyte surface by screen printing $(La_{0.80}Sr_{0.20})_{0.95}CoO_{3-x}$ (LSC) cathode ink (Nexceris). After the screen-printing process, the cell was dried in air at room temperature for 24 h. The cathode layer was deposited twice. The resulting active electrode area was 0.6 cm^2. The cathode side was attached to the Pt mesh using Ag paste (Nexceris). The cell was mounted on top of the alumina tube and sealed with Ceramabond 552 (AREMCO) paste. The sealant was dried in air for 4 h before it was tested.

The test setup configuration of the button-typed MS-SOFC is illustrated in Fig. S.3. The cell was heated to 800 °C at a heating rate of 1.5 °C min^{-1}. During cell heating, 80 sccm of H_2 and 20 sccm of N_2 (with 3% of H_2O) flowed into the anode, while the cathode was exposed to 100 sccm of air. The OCV of the cell was measured. After the cell temperature reached 800 °C, the temperature was held for 6 h for the *in-situ* sintering

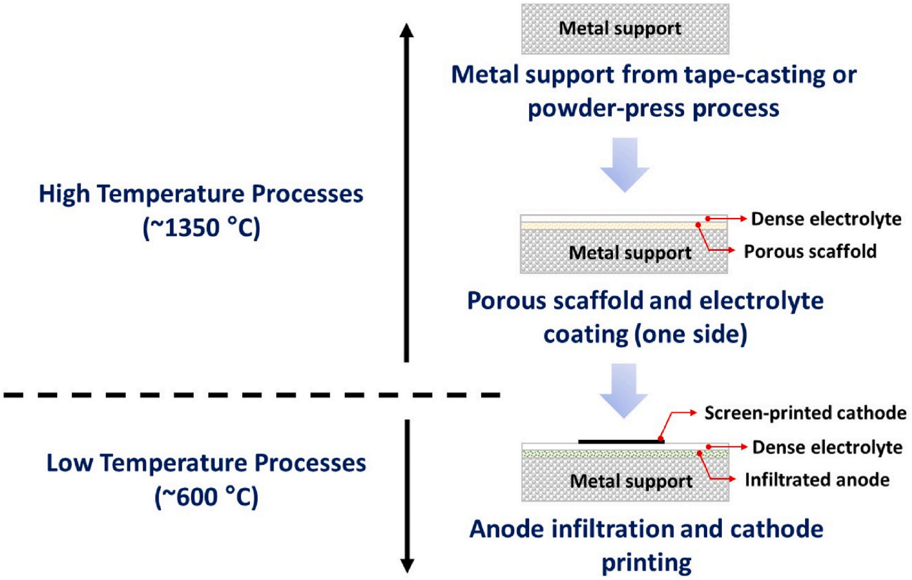

Fig. 1. MS-SOFC fabrication steps. Reproduced from Ref. [34] with permission from the International Journal of Hydrogen Energy.

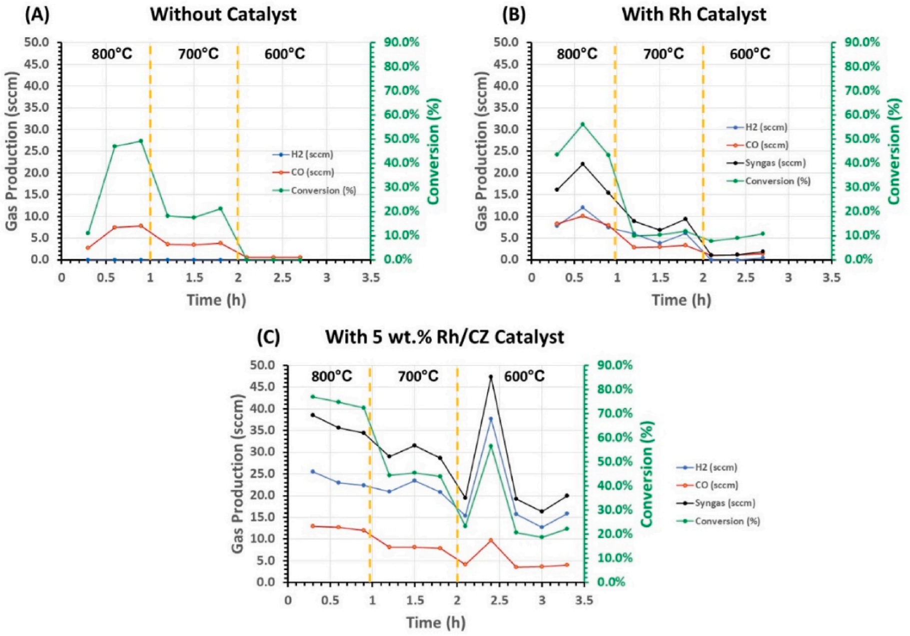

Fig. 2. Catalytic activity of the YSZ scaffold under 45 vol% of ethanol solution (S/C = 2) at 800-600 °C: (A) without catalyst, (B) with infiltrated Rh catalyst, and (C) with infiltrated 5 wt% Rh/CZ catalyst.

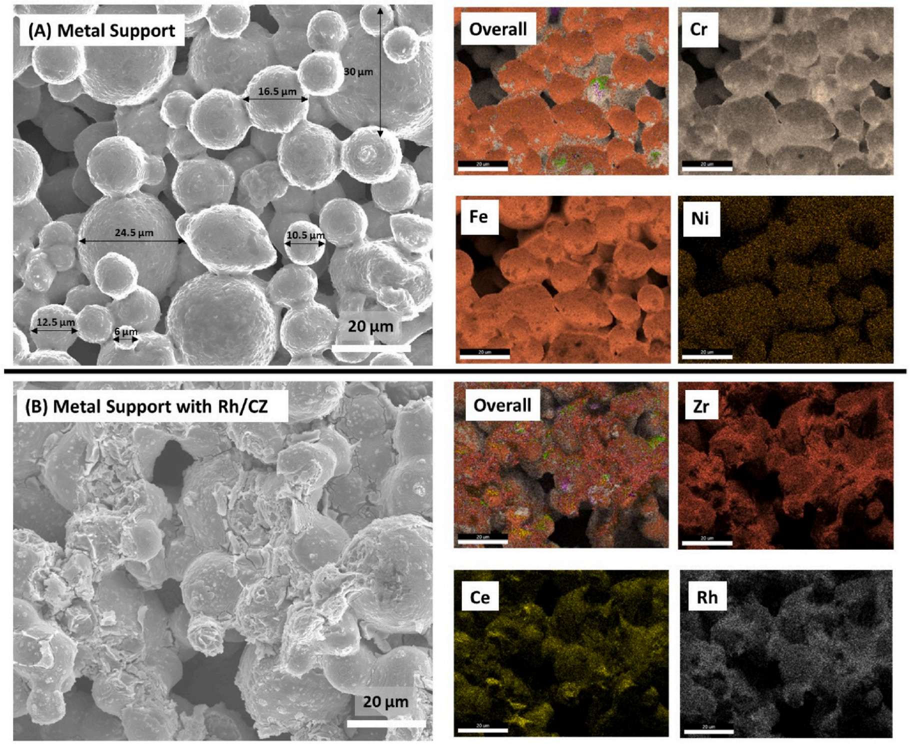

Fig. 3. SEM and EDS map analysis of: (A) the metal support without catalyst (showing the high range of particle size distribution), and (B) with infiltrated Rh/CZ catalyst.

of the LSC cathode. The electrochemical performance of the button cell was measured using a custom homemade fuel cell test system as we described in our previous publications [15,18,36]. The test system consists of mass flow controllers (Brooks 8580E), a DC electric load (BK precision 8500), and an Autolab electrochemical workstation (Metrohm Autolab M101). Electrochemical impedance spectra were measured under OCV conditions in the frequency range 0.01 Hz–100 kHz with the amplitude of the input sinusoidal signal of 10 mV. Initial cell performance tests were conducted under humidified H_2 fuel at 600–700 °C. Both impedance and the IV test were measured and compared with the MS-SOFC without 5 wt % Rh/CZ catalyst under the same operating conditions. After obtaining the initial performance using H_2 gas, simulated syngas consisting of 50 sccm N_2, 50 sccm H_2, and 7 sccm of CO flowed into the cell as a reference fuel at 600 °C. The 45 vol% aqueous ethanol was introduced using a calibrated peristaltic pump with 50 sccm of N_2 as a carrier gas at the same temperature. The impedance and IV data were also measured for the various fuel conditions. Cell stability test at constant current was performed using 45 vol % aqueous ethanol at 600 °C. The current density was determined after the IV measurement, where the cell voltage was at ~0.7 V. The stability test was conducted continuously until the cell was deactivated or showed a significant decline in voltage.

2.4. Post-test cell characterization

Post mortem cell characterization was conducted following the stability test under the constant current condition. The cell was visually observed on both its anode and cathode surfaces to check for the presence of coking and any sign of cracking or damage to the cell. In addition, SEM and EDS mapping were conducted on the cell. TPO experiments were carried out on the spent MS-SOFC using an integrated TG-DSC-MS system (Netzsch STA 449 F5 Jupiter coupled with a QMS 403 D Aëolos). Typically, around 15 mg of spent fuel cell materials were loaded in an alumina (Al_2O_3) crucible and analyzed from 35 to 700 °C with a ramp rate of 10 °C min^{-1} under an O_2/N_2 gas mixture (10 vol% O_2) at a total flow rate of 60 mL/min. The gases that evolved during the analysis were identified by the coupled MS. Specifically, the CO_2 signal was normalized based on the weight of the sample in the crucible.

3. Results and discussion

3.1. Catalyst characterization

3.1.1. Rh/CZ on YSZ reforming performance

The YSZ scaffold without the catalyst (Fig. 2 (A)) shows ~45% carbon conversion at 800 °C due to the ethanol decomposition at high temperature. Conversion diminished when the temperature was decreased to 600 °C due to the slower kinetics. However, almost no H_2 is produced at temperatures ranging from 600 and 800 °C because YSZ is catalytically inactive for ESR. The YSZ scaffold with Rh catalyst (Fig. 2 (B)) shows a slightly higher conversion (~50%), and a small amount of syngas production (~15 sccm) at 800 °C. At 600 °C, syngas production dropped to almost zero. This finding shows that Rh without support is not active for ESR because it does not have good oxygen storage capacity, which matches our previous ESR test using the fixed-bed reactor [18].

The YSZ scaffold with Rh/CZ catalyst (Fig. 2 (C)) shows a high conversion (~70%) with total syngas production of ~35 sccm at 800 °C. When the temperature is decreased to 600 °C, syngas production is ~20 sccm. Even though the performance is much better than the blank YSZ or Rh pellet, it is lower than the typical syngas production rate requirement for a SOFC operating at the low cell voltage (~50 sccm). At this low cell voltage operating condition, excess syngas is necessary to avoid mass transfer limitation to meet the corresponding high current density requirement. At 600 °C and using the Rh/CZ catalyst, the H_2:CO ratio is 3:1. The amount of CO is still too high and may degrade the SOFC in the long run via disproportionation of CO (Boudouard reaction) that leads to carbon formation. Nevertheless, the reforming data shows that the Rh/CZ catalyst synthesized with the infiltration method within the scaffold is catalytically active towards the ESR condition and can provide sufficient syngas for the standard fuel cell operation (e.g., the cell is operating at the voltage higher than 0.7 V). Thus, it can be applied to the MS-SOFC tests.

3.1.2. Rh/CZ structures and morphology

Fig. S.4 shows XRD patterns of the infiltrated Rh/CZ catalyst on the stainless steel support. The reduced sample shows stronger intensity due to the higher degree of crystallization from the reduction process. The XRD data shows all the main peaks of ceria-zirconia (CZ), which agree with the XRD patterns from the reference sample of commercial CZ (Sigma-Aldrich). Meanwhile, diffraction peaks for the metallic Rh phase are not detected for the infiltrated Rh/CZ catalyst on the stainless steel support following reduction. This XRD amorphous characteristic of our Rh nanoparticles indicates that they are highly dispersed within the stainless-steel metal support. The main diffraction peaks of the CZ phase from the infiltrated Rh/CZ sample are shifted to lower 2-theta angles relative to the reference material. This shifting is caused by the difference in stoichiometry between the infiltrated Rh/CZ ($Ce_{0.9}Zr_{0.1}O_2$) and the commercial CZ samples ($Ce_{0.5}Zr_{0.5}O_2$). Infiltration is performed after the ultrasonication process of the precursors in methanol because the ZrO_2 precursor is difficult to dissolve and tends to form a deposit at the bottom of the vial. Therefore, there is a high chance that the actual stoichiometry of the infiltrated Rh/CZ catalyst is different from the calculated formula, so that we ended up with a Ce-rich phase with a Ce:Zr ratio of 9:1 instead of the calculated ratio of 7:3, which makes the peak shift more apparent [37].

According to the literature, Ce has a high oxygen storage capacity, but it tends to be unstable at an elevated temperature due to sintering. Zr

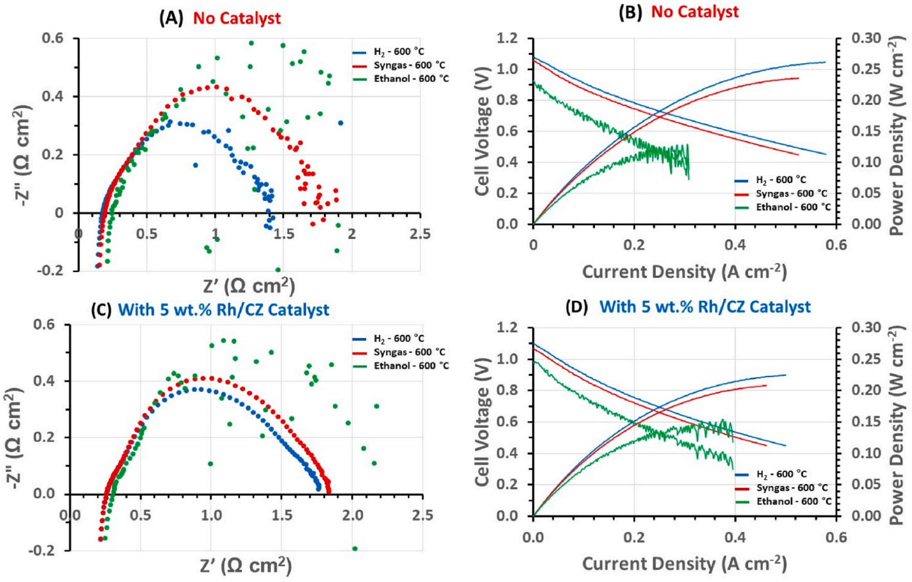

Fig. 4. Initial impedance and IV data of the MS-SOFC with and without 5 wt% Rh/CZ catalyst at 600 °C under various fuels (H_2, simulated syngas, and 45 vol% ethanol solution).

can be used to stabilize Ce by preventing sintering [38]. However, the oxygen storage capacity of Ce decreases as the Zr concentration increases for the CZ support [39]. Since our operating temperature is relatively low for reforming (600 °C), the catalyst deactivation effect from particle sintering would not be significant. Consequently, a high Ce:Zr ratio (9:1) would be favorable for our application.

Fig. 3 shows the SEM and EDS map analysis of the metal support before and after catalyst infiltration. The SEM image reveals that the metal support has a high degree of porosity with a broad particle size distribution between 6 and 30 μm. The EDS map confirms the majority of components of a typical 430 stainless steel (Fe, Cr, and Ni) (Fig. 3 (A)). The SEM and EDS analysis of the metal support after the catalyst infiltration shows that the Rh/CZ catalyst is uniformly coated and well-dispersed over the metal support particles (Fig. 3 (B)).

3.2. Ethanol steam reforming of metal-supported SOFC

3.2.1. Electrochemical and reforming performances

Fig. S.5 shows the initial cells performance tests under humidified H_2 at 600–700 °C for the cell with and without 5 wt% Rh/CZ catalyst. The impedance data under the OCV condition show that the cells with and without the catalyst display a similar ohmic resistance (i.e., the impedance at high frequency) under H_2 condition (Fig. S.5 (A and B)). A similar trend is also shown when we switched the fuel to simulated syngas (50 sccm of $H_2 + 7$ sccm of CO), and 45 vol% ethanol solution ($S/C = 2$) at 600 °C (Fig. 4). This evidence shows that the infiltration process of the Rh/CZ catalyst does not affect the ohmic resistance of the cell because this is mostly influenced by the ionic resistance of the electrolyte and the Rh/CZ precursor only fills the void space in the metal support. However, the total impedance value of the cell with 5 wt% Rh/CZ is higher than the cell without the catalyst. The infiltrated catalyst contains a non-conductive ZrO_2 component. As the non-electrically conductive ZrO_2 fills the void space of the metal support, the anode conductivity would decrease, which is responsible for the increased total impedance.

Fig. 4 (A and C) show that upon switching the fuel from the humidified H_2 to syngas, the cell without the catalyst shows a higher total impedance increase (~0.4 Ω cm^2), compared to the cell with 5 wt% Rh/CZ, which only shows ~0.1 Ω cm^2 total impedance increase. Upon switching the fuel to the ethanol solution, the low-frequency impedance of the cells with and without the catalyst becomes unstable. The ethanol solution needs to be internally reformed at the anode before the synthesis gas can be electrochemically oxidized. Because the low-frequency impedance is highly correlated to the mass transport phenomena of the cell, this increased degree of low-frequency impedance data scattering is caused by insufficient production and transport of synthesis gas at the anode under the ethanol solution fuel. However, it is essential to point out that the cell's low-frequency impedance with the catalyst shows a much lower degree of data scattering than the cell without the catalyst, indicating that the presence of the Rh/CZ catalyst within the anode improves the cell's internal ethanol reforming performance.

The cell with and without 5 wt% Rh/CZ catalyst show a similar IV performance trend under H_2 fuel at different operating temperatures (Fig. S.5 (C and D)), suggesting that both cells are comparable. Fig. 4 (B) shows the IV plots of the cell without the catalyst at 600 °C using various fuels. Under the humidified H_2 condition, its OCV value is 1.09 V which is very similar to the theoretical cell potential value of 1.10 V. When the fuel is changed from the humidified H_2 to simulated synthesis gas, the OCV value drops by 0.02 V due to the lower hydrogen partial pressure according to the Nernst equation. Finally, under the ethanol solution fuel, the OCV value decreased to 0.9 V due to the further reduced hydrogen partial pressure from the low internal reforming activity of ethanol. Consequently, the current density at 0.3 V is only ~0.3 A cm^{-2} with a highly fluctuating voltage at a higher current density region of the IV plot. Unlike the cell without the catalyst, according to Fig. 4 (D), the cell with the Rh/CZ catalyst under the ethanol solution fuel condition shows the higher OCV value of 1.0 V and the higher current density of 0.4 A cm^{-2} at 0.3 V with a lower degree of cell voltage fluctuation. These improved IV performances for the cell with the catalyst indicate the improved internal ethanol reforming activity. To directly measure the internal ethanol reforming activity of the cells, the anode effluent gas stream from the cell with and without the Rh/CZ catalyst was analyzed using the GC at the OCV condition (i.e., the zero load condition). Fig. 5 shows the reforming activity of the cell with and without the catalyst at the OCV condition. According to Fig. 5 (A), the cell without the catalyst shows a carbon conversion of only about 40% with a synthesis gas production rate of 20 sccm. On the other hand, according to Fig. 5 (B), the cell with the catalyst shows a carbon conversion of 55% with a synthesis gas production rate of 30 sccm. Thus, the introduction of the catalyst within the anode design of the MS-SOFC improves the synthesis gas production rate by 50%, which increases the hydrogen partial pressure under the ethanol solution fuel condition. With this higher hydrogen partial pressure, the cell with the catalyst under the ethanol solution fuel can achieve a higher OCV value, higher current density, and more stable IV characteristics.

The constant current stability test was performed following the IV test and is shown in Fig. 6. We set the current density at 100 mA cm^{-2} for the cell without the catalyst and 140 mA cm^{-2} for the cell with 5 wt% Rh/CZ catalyst, which equals the cell voltage of 0.7 V. The cell without the catalyst completely deactivates after only 1.2 h. We attempted to recover the cell's activity by feeding humidified H_2. However, its OCV was constant at 0.1 V and would not recover (data not shown). This result indicates a permanent cell deactivation from either coking or structural damage. Meanwhile, the cell with 5 wt% Rh/CZ shows a stable performance over 40 h. Since we did not observe any signs of deactivation, we ran the cell for another 90 h before the cell voltage fluctuated and deactivated due to failure of the sealing system. The cell with 5 wt% Rh/CZ shows a slow voltage deactivation rate of 1.5 mV h^{-1}, which indicates the success of the infiltrated catalyst layer.

Fig. 7 shows the corresponding catalytic activity of the cells during

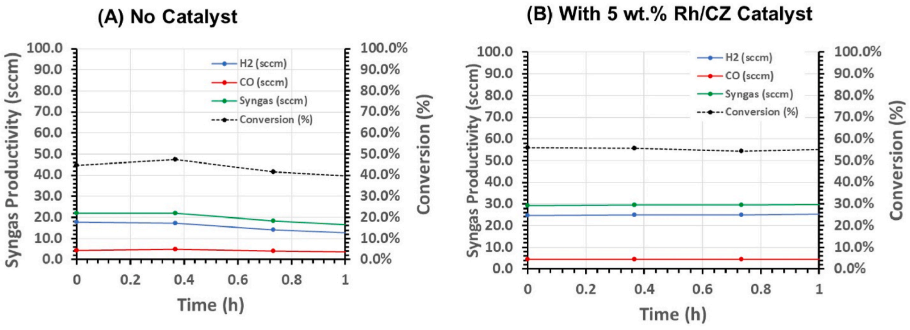

Fig. 5. Catalytic activity of the MS-SOFC under 45 vol% of ethanol solution ($S/C = 2$) at 600 °C in OCV condition: (A) without catalyst, (B) with 5 wt% Rh/CZ catalyst.

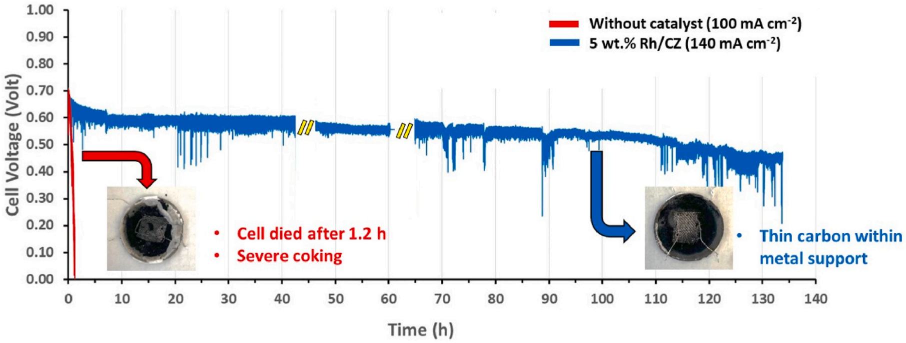

Fig. 6. Stability data of MS-SOFC under the constant current density and 45 vol% of ethanol solution (S/C = 2) at 600 °C.

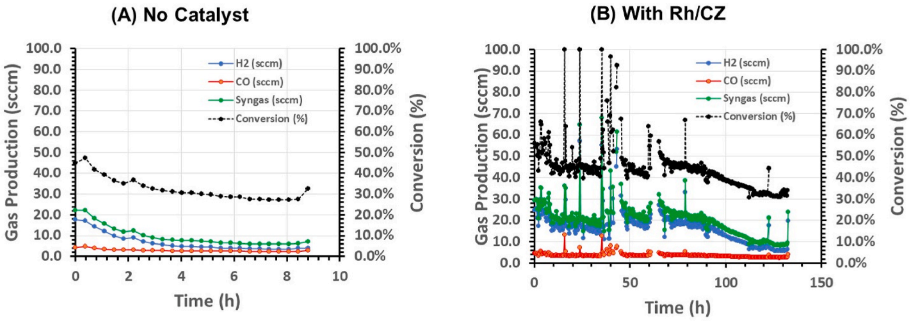

Fig. 7. Catalytic activity of the MS-SOFC under 45.vol% of ethanol solution (S/C = 2) at 600 °C under OCV (t = 0–1 h) and constant current density condition (t = >1 h): (A) without catalyst, (B) with 5 wt% Rh/CZ catalyst.

the long-term stability test. The cell without the catalyst shows initial synthesis gas productivity of ~20 sccm during the first hour of the test. However, the synthesis gas productivity rapidly declined to ~7 sccm at the ninth hour of the test, which is responsible for the rapid cell deactivation shown in Fig. 6. The cell with 5 wt% Rh/CZ shows that the average synthesis gas production is about 30 sccm (26 sccm of H_2 and 4 sccm of CO) at the OCV condition. During the first 80 h of the cell test under applied constant current, syngas production only decreased from 30 sccm to 24 sccm. Interestingly, the cell mostly consumes hydrogen during the constant load condition where the CO flow rate maintains at 4 sccm, which suggests that H_2 is easier to be electrochemically oxidized than CO.

3.2.2. *Post-test characterization*

SEM and EDS mapping analyses were performed following the constant current long-term test. Fig. 8 (A) shows the SEM and EDS analysis of the cell without the catalyst at the metal support surface. EDS maps show the presence of elemental carbon (purple color) within the entire anode and metal support region, which is the main cause of the cell deactivation during the long-term test under the ethanol fuel condition (Fig. 8 (A-II and A-III)). The coking on the cell blocks the active sites of the Ni anode, causing the lack of syngas production, as shown in Fig. 7 (A) and eventually leading to a drop in cell voltage. Meanwhile, SEM and EDS analysis of the cell with 5 wt% Rh/CZ catalyst revealed a significantly lower amount of elemental carbon within the cell (Fig. 8 (B-II and B-III)). The image of the anode surface of the spent cell only shows a thin carbon layer (Fig. 8 (B–I), inset). To quantify the amount of coking, TPO experiments were performed using an integrated TG-DSC-MS system, as shown in Fig. 8 (C). The cell without reforming catalyst shows a high CO_2 signal peak between 550 and 700 °C, corresponding to the temperature range for oxidation of "hard" carbons [40]. Meanwhile, the 5 wt% Rh/CZ catalyst cell only shows a small CO_2 peak around this high-temperature region. On the other hand, the cell with 5 wt% Rh/CZ catalyst shows other CO_2 peaks within the 200–300 °C region, corresponding to the temperature range for oxidation of "light" carbons [41]. This TPO data suggests that the cell with 5 wt% Rh/CZ catalyst has a better selectivity to form "light" carbons. This "light" carbon is easier to remove compared to "hard" carbon because it requires lower oxidation temperatures. Based on the area of the CO_2 peaks signal, we calculated the amount of carbon present in the cell without catalyst to be 0.6 wt%, while the amount of carbon in the cell with 5 wt% Rh/CZ is 0.06 wt. This data indicates that the infiltrated 5 wt% Rh/CZ on the metal-supported SOFC can effectively protect the anode from deactivation due to coking.

4. Conclusions

A 5 wt% Rh/CZ catalyst was successfully introduced into the MS-SOFC by a series of precursor infiltration and heat treatment processes. As we have demonstrated in our previous work [18], the reforming catalyst functional layer can effectively enhance the ethanol reforming activity by producing a high rate of syngas that improves the electrochemical performance of the MS-SOFC. The XRD and catalyst activity data show that the Rh/CZ catalyst can be synthesized by mixing the metal precursors and infiltrating them on an inert metal support of the MS-SOFC. This is a promising technique for the catalyst integration because it does not require an external reforming reactor or an additional internal catalyst layer that increases the total fuel system volume. Under direct feeding conditions of an ethanol solution fuel, the MS-SOFC without the catalyst shows a more scattered impedance, lower OCV, fluctuating cell voltage, and lower maximum current density than the MS-SOFC with the 5 wt% Rh/CZ catalyst. At 0.3 V, the cell without the catalyst displays a maximum current density of ~0.3 A cm^{-2}. In contrast, the cell with 5 wt% Rh/CZ catalyst shows a maximum current density of 0.4 A cm^{-2} at the same cell voltage. The cell with the infiltrated 5 wt% Rh/CZ also shows much improved stability during the long-term test under the constant current condition for 130 h. Post-test analysis using SEM, EDS, and TPO suggested that the infiltrated 5 wt%

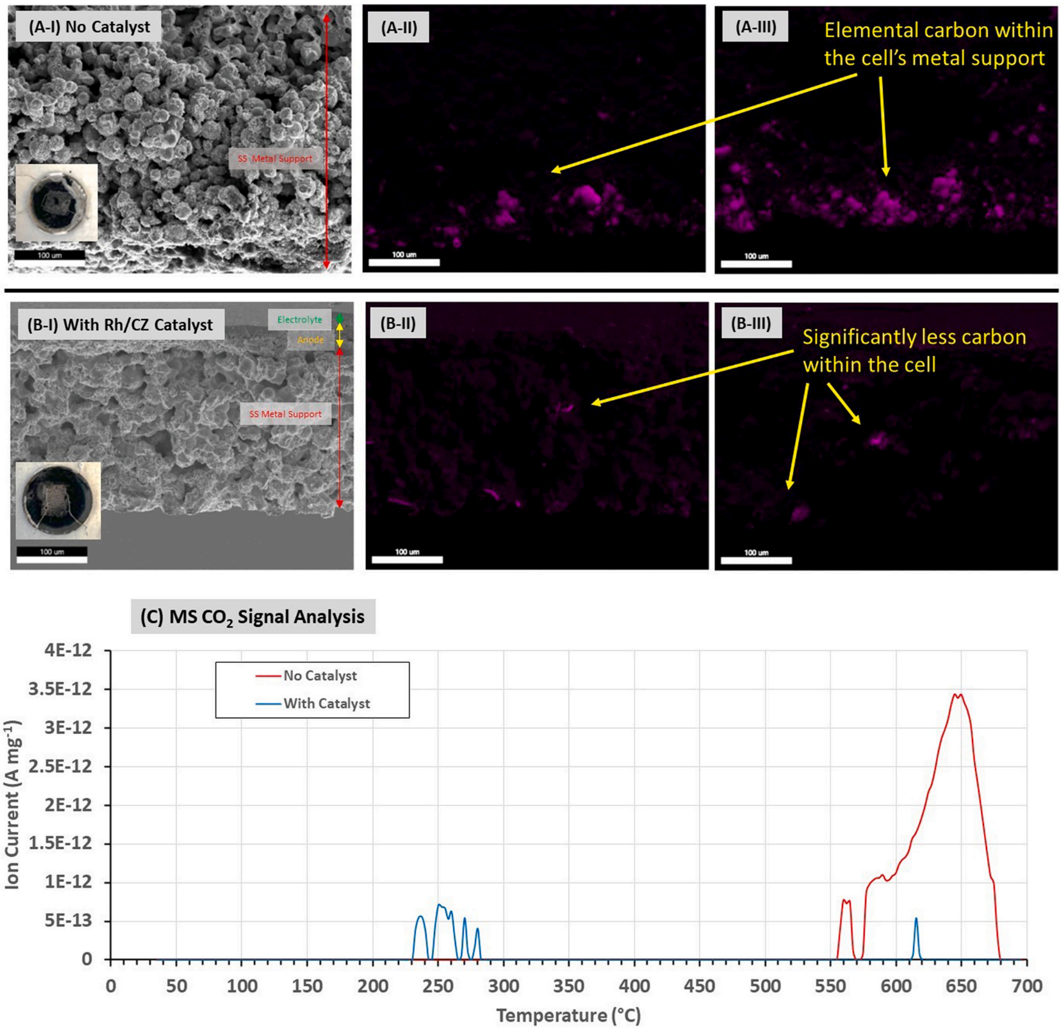

Fig. 8. (A–I) SEM image of the spent cell without catalyst. The inset image is the photograph of the anode surface, (A-II and A-III) EDS elemental carbon map of the spent cell without catalyst at two different spots, (B–I) SEM image of the spent cell with Rh/CZ catalyst. The inset image is the photograph of the anode surface, (B-II and B-III) EDS elemental carbon map of the spent cell with Rh/CZ catalyst at two different spots, and (C) MS CO$_2$ signal analysis of the spent cells.

Rh/CZ catalyst on the MS-SOFC system could improve the anode's coking resistance. This result demonstrates the effectiveness of the 5 wt % Rh/CZ catalyst infiltration in an MS-SOFC system for ethanol steam reforming reaction.

CRediT authorship contribution statement

Martinus Dewa: Conceptualization, Methodology, Validation, Formal analysis, Investigation, Writing – original draft, Writing – review & editing, Visualization. **Mohamed A. Elharati:** Methodology, Formal analysis. **A. Mohammed Hussain:** Conceptualization, Methodology, Writing – review & editing, Resources, Supervision, Project administration. **Yohei Miura:** Methodology, Writing – review & editing, Resources. **Dong Song:** Methodology, Writing – review & editing, Resources. **Yosuke Fukuyama:** Methodology, Writing – review & editing, Resources. **Yoshihisa Furuya:** Methodology, Writing – review & editing, Resources. **Nilesh Dale:** Conceptualization, Resources. **Xianghui Zhang:** Formal analysis, Investigation. **Oscar G. Marin-Flores:** Formal analysis, Investigation. **Di Wu:** Formal analysis. **M. Grant Norton:** Writing – review & editing. **Su Ha:** Conceptualization, Methodology, Formal analysis, Writing – original draft, Writing – review & editing, Supervision, Project administration, Funding acquisition.

Declaration of competing interest

The authors declare the following financial interests/personal relationships which may be considered as potential competing interests:

Su Ha reports financial support was provided by The Nissan Motor Corporation Limited via Nissan Technical Centre North America. Su Ha reports a relationship with The Nissan Motor Corporation Limited via Nissan Technical Centre North America that includes: funding grants.

Acknowledgments

This work was financially supported by the Nissan Motor Corporation Limited via Nissan Technical Centre North America and the United State National Science Foundation under award number CBET-2050691. The authors acknowledge the O.H. Reaugh Laboratory at Washington State University for using its facility to perform activity tests.

Special thanks to the Franceschi Microscopy and Imaging Center (FMIC) at WSU for the use of their electron microscope expertise and facilities.

Appendix A. Supplementary data

Supplementary data to this article can be found online at https://doi.org/10.1016/j.jpowsour.2022.231625.

References

[1] A. Hagen, X. Sun, B.R. Sudireddy, Å.H. Persson, J. Electrochem. Soc. 167 (2020).

[2] M. Chen, B.H. Kim, Q. Xu, O.J. Nam, J.H. Ko, J. Eur. Ceram. Soc. 28 (2008) 2947–2953.

[3] M.C. Tucker, J. Power Sources 195 (2010) 4570–4582.

[4] M.C. Tucker, G.Y. Lau, C.P. Jacobson, L.C. DeJonghe, S.J. Visco, J. Power Sources 171 (2007) 477–482.

[5] M.H. Pihlatie, A. Kaiser, M. Mogensen, M. Chen, Solid State Ionics 189 (2011) 82–90.

[6] M.C. Tucker, G.Y. Lau, C.P. Jacobson, L.C. DeJonghe, S.J. Visco, J. Power Sources 175 (2008) 447–451.

[7] M.C. Tucker, Energy Technol. 5 (2017) 2175–2181.

[8] S.D. Stephens-Romero, T.M. Brown, J.E. Kang, W.W. Recker, G.S. Samuelsen, Int. J. Hydrogen Energy 35 (2010) 4652–4667.

[9] J.-G. Kim, M. Kuby, Int. J. Hydrogen Energy 37 (2012) 5406–5420.

[10] J.J. Brey, R. Brey, I. Contreras, A.F. Carazo, Int. J. Hydrogen Energy 39 (2014) 4116–4122.

[11] J.J. Brey, R. Brey, A.F. Carazo, Int. J. Hydrogen Energy 42 (2017) 13382–13388.

[12] J.J. Brey, A.F. Carazo, R. Brey, Renew. Sustain. Energy Rev. 82 (2018) 2893–2899.

[13] M. Muratori, B. Bush, C. Hunter, M. Melaina, Energies 11 (2018).

[14] E. Commission, Off. J. Eur. Union 57 (2014).

[15] K. Zhao, X. Hou, Q. Bkour, M.G. Norton, S. Ha, Appl. Catal. B Environ. 224 (2018) 500–507.

[16] S.P.S. Shaikh, A. Muchtar, M.R. Somalu, Renew. Sustain. Energy Rev. 51 (2015) 1–8.

[17] J.B. Goodenough, Y.-H. Huang, J. Power Sources 173 (2007) 1–10.

[18] M.A. Elharati, M. Dewa, Q. Bkour, A. Mohammed Hussain, Y. Miura, S. Dong, Y. Fukuyama, N. Dale, O.G. Marin-Flores, S. Ha, Energy Technology, 2020.

[19] B. Huang, S.R. Wang, R.Z. Liu, T.L. Wen, J. Power Sources 167 (2007) 288–294.

[20] X.-F. Ye, B. Huang, S.R. Wang, Z.R. Wang, L. Xiong, T.L. Wen, J. Power Sources 164 (2007) 203–209.

[21] B. Huang, S.R. Wang, R.Z. Liu, X.F. Ye, H.W. Nie, X.F. Sun, T.L. Wen, J. Power Sources 167 (2007) 39–46.

[22] Z. Xiong, Z. Fang, L. Jiang, H. Han, L. He, K. Xu, J. Xu, S. Su, S. Hu, Y. Wang, J. Xiang, Fuel (2022) 314.

[23] X. Chang, B. Liu, H. Xia, R. Amin, Appl. Surf. Sci. 442 (2018) 342–351.

[24] G. Chen, X. Dong, B. Yan, J. Li, K. Yoshikawa, L. Jiao, Appl. Energy 305 (2022).

[25] R. Amin, B. Liu, Z.B. Huang, Y.C. Zhao, Int. J. Hydrogen Energy 41 (2016) 807–819.

[26] R. Amin, B. Liu, S. Ullah, H.Z. Biao, Int. J. Hydrogen Energy 42 (2017) 21607–21616.

[27] N. Morlanés, G. Lezcano, A. Yerrayya, J. Mazumder, P. Castaño, Chem. Eng. J. 433 (2022).

[28] F.M. Bkangmo Kontchouo, K. Sun, C. Li, Z. Fu, S. Zhang, L. Xu, X. Hu, J. Energy Inst. 101 (2022) 32–44.

[29] Z. Zhan, S. Barnett, Solid State Ionics 176 (2005) 871–879.

[30] J. Qu, W. Wang, Y. Chen, X. Deng, Z. Shao, Appl. Energy 164 (2016) 563–571.

[31] Z. Tao, G. Hou, N. Xu, Q. Zhang, Int. J. Hydrogen Energy 39 (2014) 5113–5120.

[32] W. Wang, J. Qu, P.S.B. Julião, Z. Shao, Energy Technol. 7 (2019) 33–44.

[33] J. Ma, C. Jiang, P.A. Connor, M. Cassidy, J.T.S. Irvine, J. Mater. Chem. 3 (2015) 19068–19076.

[34] M. Dewa, W. Yu, N. Dale, A.M. Hussain, M.G. Norton, S. Ha, Int. J. Hydrogen Energy 46 (2021) 33523–33540.

[35] M. Cimenti, J. Hill, Energies 2 (2009) 377–410.

[36] K. Zhao, Q. Bkour, B.-H. Kim, M.G. Norton, S. Ha, Energy Technol. 7 (2019) 48–52.

[37] C. Liang, J. Qiu, Z. Li, C. Li, Nanotechnology 15 (2004) 843–847.

[38] T.E.E. Mamontov, R. Brezny, M. Koranne, S. Tyagi, J. Phys. Chem. B 104 (2000) 11110–11116.

[39] H. Li, Q. Zhu, Y. Li, M. Gong, Y. Chen, J. Wang, Y. Chen, J. Rare Earths 28 (2010) 79–83.

[40] G.N.W. Jiang, K. Zaghib, K. Kinoshita, Thermochim. Acta 351 (2000) 85–93.

[41] Y. Li, Y.-S. Hu, H. Li, L. Chen, X. Huang, J. Mater. Chem. 4 (2016) 96–104.